

RTIndex: Exploiting Hardware-Accelerated GPU Raytracing for Database Indexing

Justus Henneberg
Johannes Gutenberg University
Mainz, Germany
henneberg@uni-mainz.de

Felix Schuhknecht
Johannes Gutenberg University
Mainz, Germany
schuhknecht@uni-mainz.de

ABSTRACT

Data management on GPUs has become increasingly relevant due to a tremendous rise in processing power and available GPU memory. Just like in the CPU world, there is a need for performant GPU-resident index structures to speed up query processing. Unfortunately, mapping indexes efficiently to the highly parallel and hard-to-program hardware is challenging and often fails to yield the desired performance and flexibility. Therefore, we advocate to take a different route. Instead of proposing yet another hand-tailored index, we investigate whether we can exploit an indexing mechanism that is already built into modern GPUs: The raytracing hardware accelerator provided by NVIDIA RTX cards. To do so, we re-phrase database indexing as a raytracing problem, where we express the dataset to be indexed as primitives in a scene, and queries as rays. In this combination, coined **RX** in the following, lookups are performed as intersection tests in hardware by dedicated raytracing cores. To analyze the pros, cons, and usefulness of the raytracing pipeline for database indexing, we carefully evaluate **RX** along *twelve* dimensions: We first identify the optimal setup of the pipeline by evaluating different options regarding (1) how to express keys, (2) which primitives to use for that, (3) how to formulate point/range queries against these, and (4) how to update the index. Continuing with the best setup, we compare **RX** against a set of software-implemented GPU-resident index structures while varying (5) the number of inserts and queries, (6) the order of the data, (7) the batch size, (8) the hit/miss ratio, (9) the selectivity of range queries, (10) the key size, and (11) the distribution of inserts and queries. Finally, we evaluate (12) the impact of three different GPU generations on the performance. Our results show that **RX** is competitive against traditional counterparts in a variety of situations.

Artifact Availability:

The source code, data, and/or other artifacts have been made available at <https://gitlab.rlp.net/juhenneb/rtindex>.

1 INTRODUCTION

The research of recent years has shown that implementing performant index structures for highly-parallel GPU architectures is a challenging task [1–7, 17, 21, 24, 25, 29, 32, 33, 39, 44, 49, 52, 53]. In this work, we therefore investigate the question whether we really have to go down that road. Can we maybe utilize the hardware indexing mechanism that is *already integrated* in modern GPUs?

1.1 Hardware Accelerated Indexing on GPUs

This indexing mechanism appears on NVIDIA’s RTX workstation and consumer GPUs in form of a *raytracing hardware accelerator*. In

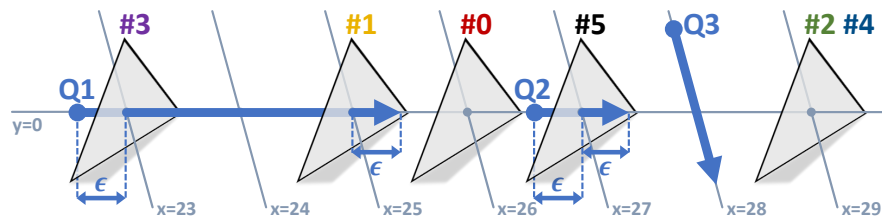
its original purpose, this accelerator enables rendering of ray-traced scenes in real time at a high frame rate. The concept is simple: A 3D scene contains a set of primitives, such as triangles, against which a set of directed rays can be fired. The core goal is to detect collisions between the fired rays and the primitives in the scene, e.g., to render reflections, shadows, or to determine ambient occlusion. To speed up this collision detection, RTX cards build a so called *bounding volume hierarchy (BVH)* over the primitives. With the BVH, the GPU can execute the collision test in hardware for a large number of rays in parallel using specialized raytracing cores that exist solely for this purpose.

At the heart, the aforementioned concept is nothing but a hardware-accelerated indexing mechanism. While the primitives in the scene resemble a dataset, the BVH serves as an auxiliary index structure on top of it. Casting a ray resembles a lookup: If a ray intersects with a primitive, the lookup returns a value associated with the primitive. This opens the possibility to map other indexing problems, such as database indexing, to this mechanism, and to exploit the built-in hardware acceleration for fast lookups. To create a secondary index on a table column, we express all keys of the column as 3D primitives, arranged by their keys in the coordinate system of the scene. We associate each primitive with the rowID of the corresponding entry in the table, which is retrieved when a ray hits the primitive. To perform a query, we fire a ray through the area of interest (small for point queries, larger for range queries), let the hardware detect all collisions, and return all associated rowIDs.

Unfortunately, expressing database indexing using this raytracing mechanism is not as straight-forward as it sounds at first glance and comes with a surprising amount of decisions to make and limitations to overcome. First of all, to realize the mapping, we use the powerful but non-trivial OptiX [16, 37] computing API, which allows us to program the raytracing pipeline freely. As OptiX provides numerous variants and options to set up the scene, for example in the types of primitives to use and the way intersection tests are performed, we can identify several drastically different ways to express database indexing in it. Second, the library and the hardware impose certain restrictions that we have to respect. For example, OptiX supports only single-precision floating-point numbers, while we want to index up to 64-bit wide integer keys. Consequently, we have to work around this problem, and again, there are multiple different ways to do so. Third, the raytracing mechanism is a proprietary implementation by NVIDIA, where details about the internal structure and behavior are not available to the public to the best of our knowledge. Therefore, it is highly unclear how well the problem of database indexing maps to the architecture and how it reacts to certain workloads, like dense/sparse key sets or the hit/miss ratio of queries.

rowID	Article	Category
0	Juice	26
1	Bread	25
2	Cookies	29
3	Coffee	23
4	Donuts	29
5	Wine	27

(a) Exemplary database table.

(b) Corresponding triangle arrangement for the *Category* column.Figure 1: Our indexing approach **RX** represents table entries with triangles, and realizes queries by casting rays.

1.2 Contributions and Structure of the Paper

As a consequence of these observations, in the following work, we investigate whether and in which form hardware accelerated indexing can be used to realize database indexing on GPUs. We organize our work along *twelve* different dimensions composed of *four* configuration dimensions and *eight* experimental dimensions. In summary, we make the following contributions:

In Section 2, we first present how to re-phrase database indexing as a raytracing problem. Based on that, we discuss our implementation of the concept, coined **RX** in the following, using the computing API OptiX. **RX** supports hardware-accelerated point and range queries on 64-bit integer columns on NVIDIA RTX cards.

In Section 3, we discuss the configuration options of **RX** along four dimensions: We implement (1) four different ways to express keys, (2) three different types of scene primitives to express the indexed dataset, (3) three different ways to express point and range queries, and (4) two different options to perform updates. Empirically, we identify the most suitable configuration that we will use throughout the rest of the paper.

In Section 4, we perform an in-depth experimental evaluation where we compare **RX** against three GPU-resident index structures along eight experimental dimensions: We vary (5) the number of inserted keys and fired queries, (6) the order of the keys and queries, (7) the batch size, (8) the hit/miss ratio, (9) the selectivity of range queries, (10) the key size, and (11) the distribution of inserts and queries. Also, we compare (12) the performance of the three latest hardware architectures.

In Section 5, we discuss all relevant related work in the field and conclude in Section 6 with the key lessons learned. These include a discussion regarding the situations in which **RX** performs well, and where its drawbacks are. Throughout the entire discussion, we put an emphasis on trying to reverse-engineer the internal behavior of the built-in raytracing mechanism. Since it is a closed-source proprietary technology, we believe our findings to be helpful for further research in this area.

2 RE-PHRASING DATABASE INDEXING AS A RAYTRACING PROBLEM

We start by re-phrasing the database indexing problem as a raytracing problem. Figure 1 visualizes the high-level principle of the approach. Assume we want to create a secondary index for the integer column *Category* of the exemplary database table shown in Figure 1a. To do so, we want to represent each key-rowID pair (k, r) of the column by a corresponding primitive. For simplicity, we limit the discussion to triangles for now and discuss other primitive

types in Section 3.4. To insert a pair (k, r) into the index, we create a triangle that is centered around the point $(k, 0, 0)$ and associate it with the rowID r . In the 3D scene, this results in a line of triangles with gaps of varying sizes in between, as visualized in Figure 1b. If an entry occurs multiple times in the table, multiple triangles will be created at the same location. After arranging all triangles in the scene, we trigger the creation of the actual index structure, which happens in a black-box fashion (see Section 2.1 for details). To answer a range query on the *Category* column, such as $[23, 25]$ (**Q1**), we can cast a ray along the line of triangles, starting at $(23 - \epsilon, 0, 0)$ and ending at $(25 + \epsilon, 0, 0)$ for some $0 < \epsilon < 1$ (see Section 2.2 for details). In Figure 1, the range query ray hits triangles **#1** and **#3**, implying that rows with rowID **1** and **3** in the original table satisfy the range predicate. We can realize a point query either as a single-key range query (**Q2**), or by casting a short ray perpendicularly to the line of triangles (**Q3**). Note that in this example, **Q3** does not hit any triangles and therefore reports a miss.

2.1 Building the Index

To build the index, we first convert each key k of the table column into a corresponding triangle T , where the point $(k, 0, 0)$ should be a part of T . One way of constructing T is by slightly offsetting each vertex in a different direction, e.g. $(k, -0.5, -0.5)$, $(k + 0.5, -0.5, 0.5)$, and $(k - 0.5, 0.5, 0.5)$. To store the triangles such that OptiX can build an index structure for them, we have arranged the triangles in a *vertex buffer*, where each triangle is implicitly defined by three successive vertices in the buffer. Each triangle is implicitly assigned a triangleID based on its offset within the vertex buffer, and in our case, the triangleID corresponds to the rowID. To actually invoke the index creation, we pass the vertex buffer to `optixAccelBuild()` to create the aforementioned BVH index over the triangles. A BVH is a tree-like data structure in which the individual triangles form the leaves of the tree. These triangles are then combined into small disjoint groups. For each group, the BVH stores a three-dimensional cuboid, called a *bounding volume*, which encloses all triangles in the group. These bounding volumes are then iteratively grouped and enclosed in the same way until only one group remains, forming the root of the tree. Figure 2 visualizes a bounding volume hierarchy for seven triangles in two dimensions.

The purpose of a BVH is to quickly rule out large amounts of possible ray-triangle intersections: If a ray does not intersect a bounding volume, it cannot possibly intersect anything within the bounding volume. Obviously, this working principle is similar to traditional tree-based database indices, such as B-Trees and R-Trees.

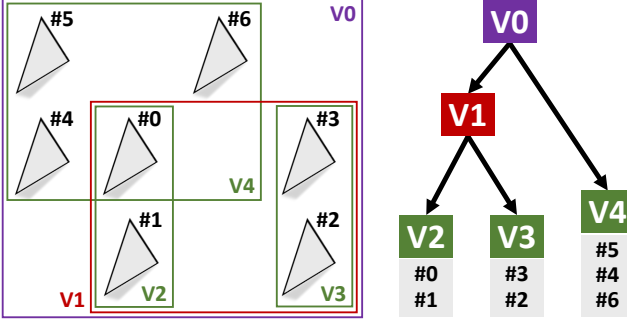


Figure 2: Exemplary bounding volume hierarchy for a (two-dimensional) triangle arrangement.

2.2 Querying the Index

Now that the BVH is prepared, let us see how we utilize OptiX to answer multiple range queries $[l^{(i)}, u^{(i)}]$ in parallel. Here, $l^{(i)}$ and $u^{(i)}$ denote the inclusive lower bound and upper bound, respectively, of the i -th range query. We formulate our batch of range queries by specifying a sequence of corresponding rays, where each ray consists of a three-dimensional *origin point* o and a *direction vector* d . A ray intersects a triangle if there exists a $t > 0$ such that the point $p = o + t \times d$ is part of the triangle. t is called the *intersection parameter*. Note that we can restrict the intersection range by providing two additional parameters, t_{\min} and t_{\max} . In this case, we will only detect intersections that also satisfy $t_{\min} < t < t_{\max}$.

To perform the actual query answering, we have to program the OptiX pipeline. The pipeline consists of multiple user-programmable functions, called *programs*, and can be launched similar to a CUDA kernel from the host CPU. First, we have to define the so-called *ray generation program*. In this program, we will fire the actual queries/rays. To do so, we invoke the API function `optixTrace()`, which receives the ray parameters and a reference to the BVH to start the hardware-accelerated tracing procedure. Precisely, for range query $[l^{(i)}, u^{(i)}]$, `optixTrace()` receives $o = (l^{(i)} - \epsilon, 0, 0)$, $d = (1, 0, 0)$, $t_{\min} = 0$, and $t_{\max} = u^{(i)} - l^{(i)} + 2\epsilon$. When we then start the pipeline, it spawns a CUDA thread for each query, where each thread calls the ray generation program to fire the corresponding ray. To handle query hits, we also have to define the so-called *any-hit program*, which is called when the tracing procedure finds a ray-triangle intersection. The any-hit program receives the `triangleID`, i.e., the offset of the triangle within the vertex buffer, which we interpret as the rowID. Note that after calling the any-hit program for a triangle T , OptiX will, by default, ignore all triangles that are further away from the ray origin than T . This effectively reduces the query range and potentially excludes triangles from being hit. To fix this problem, we override this behavior by calling `optixIgnoreIntersection()` after processing each entry.

3 DESIGN CHOICES

After discussing the core principle, let us discuss certain four fundamental design choices. We carefully evaluate all options to identify the strengths and weaknesses of each choice. Before that, let us introduce our evaluation setup first.

3.1 Experimental Setup and Methodology

We use a setup which resembles the typical usage of a secondary index, where we assume to have a table T with a certain number of rows in column layout. T consists of two columns: A *column to index* I , for which the index will be built, and a *column to project* P . The column to index I is an array containing consecutive unsigned 32-bit integers, starting at zero, where keys are shuffled arbitrarily in the column. By using a dense key set, we get a predictable number of hits when formulating range queries. The position of a key in the column forms its implicit rowID. The column to project P contains arbitrary 32-bit integers. On this table, we can execute both point and range queries, where a point query targeting the value x on the column I has the form

```
SELECT P FROM T WHERE I == x
```

whereas a range query selecting $[l, u]$ on I has the form

```
SELECT SUM(P) FROM T WHERE I >= l AND I <= u.
```

As we perform a projection on P , the rowIDs returned by the index are used to perform a lookup in P . We always answer a batch of point queries or range queries at once. The result of each query is written into a *result buffer* with as many slots as we fire queries, which can be inspected after the execution of the batch. Note that if a point query does not return a result, a reserved *miss value* is written into the result buffer instead. Unless specified otherwise, our table T has 2^{26} rows for point query experiments. As range queries take longer to be answered, we use only 2^{25} rows for the range query experiments. To generate the point query predicates, we uniformly and randomly choose x from the key set stored in column I . For range queries, we also uniformly pick a lower bound l from I and increase it by the desired number of hits to generate the upper bound u . In total, we generate 2^{27} queries for every experiment.

Each experiment consist of three phases: First, the experiment enters the *build phase*, in which we convert all keys of I to OptiX primitives and construct the BVH. The build phase is followed by the *warmup phase*, in which we evaluate the query batch once and check the results for correctness. The actual time measurements start in the *query phase*, where we launch the OptiX pipeline five more times and report the average pipeline execution time. As all data is assumed to be GPU-resident – our measurements do not include the time it takes to copy the input/output between GPU memory and main memory. All buffers are re-allocated after each experiment to reduce caching effects. This allocation time is not included in the measurements.

Regarding hardware, we use a system that contains an NVIDIA RTX 4090 GPU with 24GB of VRAM and 128 raytracing cores. This card implements the most recent Ada Lovelace architecture and is the fastest consumer RTX card currently available. In Section 4.9, we will compare the performance of three other GPUs of two older RTX architectures in comparison.

3.2 How Can We Express Keys?

The first configuration dimension centers around how we can express our keys in a 3D scene. This question is more challenging as it seems since the straightforward implementation we described

Mode	Distinct Values	Conversion Formula	ϵ	Triangles	Spheres	AABBs
Safe	2^{23}	$i \mapsto (\text{float}(i), 0.0, 0.0)$	0.5	Y	Y	Y
Unsafe	2^{24}	$i \mapsto (\text{float}(i), 0.0, 0.0)$	1	Y	N	N
Extended	2^{29}	$i \mapsto (\text{bit_cast}\langle\text{float}\rangle(2i + C), 0.0, 0.0)$	<code>nextafter()</code>	Y	N	Y
3D	2^{64}	$i \mapsto (\text{float}(i_{21:0}), \text{float}(i_{43:22}), \text{float}(i_{63:44}))$	0.5	Y	Y	Y

Table 1: Overview of our proposed order-preserving methods for converting integers to floating-point numbers.

so far omitted an inconvenient detail: OptiX only supports single-precision floating-point numbers (`float32`) to represent a vertex coordinate. As a consequence, naively storing a 32-bit integer key (or even a 64-bit key) in a coordinate will result in a loss of precision. In the following, we propose four different options to still express keys. With each presented option, we extend the supported key range, arriving at 64 bits in the end.

Safe Mode. We start with the Safe Mode, where the high-level idea is to naively express an integer key as a `float32` vertex coordinate. To understand the principle, let us look at how the integer 22 can be represented as a `float32`. The binary representation of 22 is $(10110)_2$ or $(10110.0)_2$ with a binary point. To store this number as a `float32`, we first convert it into its normalized form, which means the binary point is shifted next to the most significant bit. In our example, this resembles a shift of four positions, which we can express as

$$(10110.0)_2 = 2^4 \times (1.011)_2.$$

Here, 4 is called the **exponent** e , whereas $(1.011)_2$ is called the **significand** m . In `float32`, the (signed) exponent is represented using 8 bits, whereas the significand is composed of 24 bits¹. Unfortunately, with a significand of 24 bits, the contiguous range of non-negative integers that can be stored in a `float32` is at most 2^{24} . However, the situation is even worse: Since we have to ensure correct arithmetics when factoring in our ϵ (to start and end the ray intersection test with a distance of $\epsilon = 0.5$ to the targeted triangle as well as to the potentially neighboring triangles), we have to conservatively restrict the key range to 2^{23} . Only then, querying the very last key $2^{23} - 1$ will work, as we can express $t_{max} = 2^{23} - 1 + 0.5$ without a loss of precision. This would not be the case for $2^{24} - 1$, where $t_{max} = 2^{24} - 1 + 0.5$ is not expressible without a precision loss.

Unsafe Mode. Interestingly, we can utilize an implementation detail of OptiX to double the supported key range to 2^{24} again. As ray-triangle intersections can only occur if $t_{min} < t < t_{max}$, i.e. the boundaries are exclusive, the points $o + t_{min} \times d$ and $o + t_{max} \times d$ will *not* be subject to collision checks². This allows us to use a larger $\epsilon = 1$ while still obtaining correct results when querying the largest key $2^{24} - 1$, as $t_{max} = 2^{24} - 1 + 1$ can be expressed without a loss of precision. Note that this behavior is specific to triangles, and does not generalize to other OptiX primitives.

Extended Mode. So far, we have mapped each integer key i to its corresponding `float32` representation. This limited our supported key range to 2^{24} . However, the range of floating point numbers that can be represented by a `float32` is significantly larger than 2^{24} . To exploit this larger range, we need an order-preserving

mapping from an integer key i to a corresponding floating point number f . We propose the following mapping: Each integer key i is mapped to the $2i$ -th representable floating-point number using `std::bit_cast<float>(2i)`. While this mapping leaves sufficiently large gaps between adjacent keys to accommodate an ϵ , the distance between two neighboring `float32` is not constant. Thus, we cannot choose a constant ϵ such as 0.5. Consequently, instead of computing $f \pm \epsilon$ for a floating-point value f , we now simply use the next representable float. This float can be identified using the `std::nextafter()` function. More details will be presented in Section 3.3. Finally, note that we offset $2i$ by a constant C before casting, as not offsetting yields wrong results, probably due to implementation details related to `float32` processing. We found $C = \text{bit_cast}\langle\text{uint32_t}\rangle(0.5f)$ to work consistently for all keys up to 2^{29} .

3D Mode. While we can already express 2^{29} distinct keys in Extended Mode, a general-purpose index structure should be able to operate with 64-bit keys. To achieve this, and since vertices in OptiX are three-dimensional anyway, we now decompose the key bits into three smaller integers. We convert these integers to `float32` individually, and use them as three-dimensional coordinates to center each triangle around. In our case, for a 64-bit key i , we use the 22 least significant bits as the x coordinate (written as $x = e_{21:0}$), the next 22 bits constitute the y coordinate, and the remaining 20 bits form the z coordinate. To support 32-bit keys using this method, we extend each key to 64 bits by padding it with zeroes. By retaining $\epsilon = 0.5$, this mode is identical to Safe Mode for all keys smaller than 2^{22} . Note that this approach requires slight modifications to point queries and range queries. For point queries, the origin o now requires a three-dimensional offset. For range queries, a single ray might now be insufficient, since the triangles do not form a single “line” anymore, but are scattered across the 3D scene. Instead, we have to cast distinct rays for each integer between $l_{63:22}^{(i)}$ and $u_{63:22}^{(i)}$. If a range query spans at most 2^{22} integers, it can be answered by casting only one or two rays. Figure 4 demonstrates how to answer the range query $[l, u] = [15, 21]$ in 3D Mode. To visualize the principle in the example, we assume to have only two dimensions, where the x coordinate is determined by the two least significant bits of the corresponding key, and the y coordinate by all remaining bits. Table 4a shows the indexed keys along with their x and y coordinates in decimal representation. To answer the range query $[15, 21]$, we first split both bounds into their coordinates, i.e., $l = 15$ into $x_l = l_{1:0} = 3$ and $y_l = l_{63:2} = 3$, and $u = 21$ into $x_u = u_{1:0} = 1$ and $y_u = u_{63:2} = 5$. As the range of interest along the y -axis ranges from 3 to 5, we have to fire three corresponding rays in parallel to the x -axis. The first ray we fire starts at $x_l - \epsilon = 3 - 0.5$, the last ray ends at $x_r + \epsilon = 1 + 0.5$, whereas all intermediate rays (for $y = 4$ in this example) are unbounded.

¹Actually, only 23 bits are required for storing the significand, as it usually starts with a leading one. The single remaining bit stores the sign of the represented number.

²Note that only the DirectX raytracing specification [12] explicitly mentions this, while it does not appear in the OptiX manual.

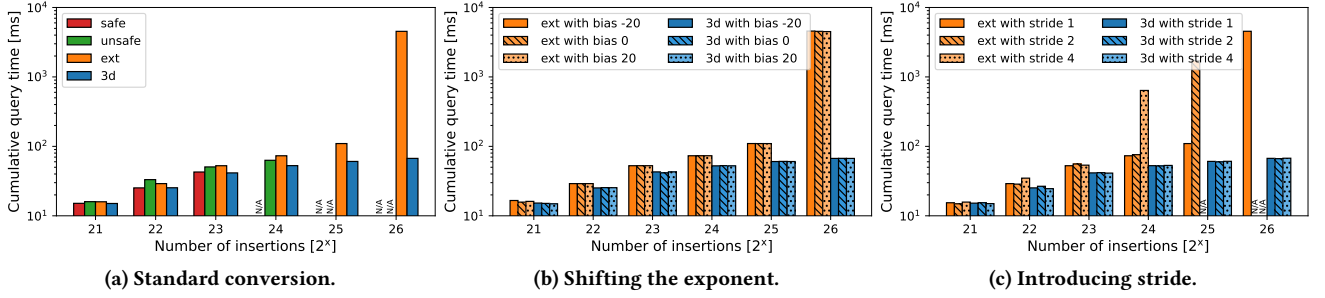


Figure 3: Effects of key conversion on lookup time. Notice the irregular behavior of Extended Mode (“ext”).

Let us now see how the four keys conversion methods perform in comparison. Figure 3a shows the accumulated lookup times when varying the build size from 2^{21} to 2^{26} .

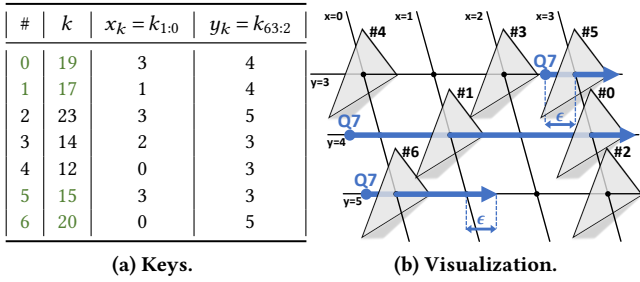


Figure 4: Answering the range query [15,21] in 3D Mode (simplified to two dimensions).

As we can see, the probe times are very similar between all four conversion methods, apart from one oddity: With Extended Mode, probing takes an extraordinary amount of time as soon as the build size exceeds 2^{25} . This is likely due to implementation details in OptiX’ internal intersection routines, the source code of which is not openly available. Nevertheless, we can hypothesize which property of the key set is responsible for the slowdown: (1) The *amount of inserted keys* could be responsible, possibly due to inefficient caching. We can immediately reject this hypothesis since the lookup times are unaffected in 3D Mode with the same amount of inserted keys. (2) The *distance between two neighboring keys* could be responsible, since it is extremely small in Extended Mode, but then we should see the slowdown regardless of the number of inserted keys, which we do not. (3) The *magnitude of keys* could be responsible, since the numbers produced in Extended Mode become very large at some point, up to around $2^{62}/10^{18}$. In contrast, other conversion methods only produce keys up to $2^{24}/10^7$. To test this hypothesis, we modify our key conversion such that it biases the float32 exponent by a fixed value b after conversion, effectively multiplying each key by 2^b . If the hypothesis was true, we should be able to see an increase in lookup time as the bias b gets bigger, which we varied in Figure 3b from -20 to 20 for Extended Mode and 3D Mode. Instead, the results show that the lookup times of the biased variants are within margin of error of the unbiased variant. (4) The *range of keys* could be responsible, i.e. the ratio q between the largest and the smallest inserted key, possibly due to internal float32 precision issues. We test this by introducing *key stride*: Instead of inserting keys 1, 2, 3, etc., we insert $1s, 2s, 3s, \dots$, with

stride parameter $s = 1, s = 2$, and $s = 4$ in Figure 3c. The results show that this hypothesis is likely true: The lookup times explode as soon as q hits 2^{26} , and for any larger q , the experiment timed out after five minutes.

Selected Configuration. In conclusion, only 3D Mode exhibits stable scaling behavior, and therefore, we will use this mode as the default key conversion method for all subsequent experiments. This allows **RX** to support signed and unsigned integer keys up to 64 bits. Another consequence of this experiment is that one should not try to index float32 and float64 columns directly, since the ratio between the smallest and largest value might be very large. Instead, the each key should be converted to an integer in an order-preserving fashion, and then indexed using 3D Mode.

3.3 How Should We Cast Rays for Queries?

Next, let us discuss and evaluate the options we have in casting rays for range queries and for point queries. Let us first look at answering a range query $[l, u]$, which also covers point queries by setting $l = u$.

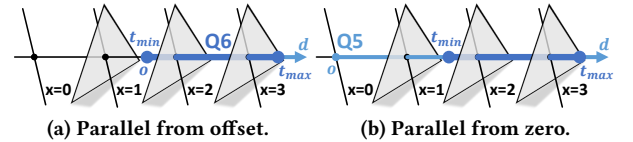


Figure 5: Two ways of expressing the range query [2, 3].

Figure 5 shows the two options we have to answer $[2, 3]$: In **Parallel from offset** (Figure 5a), which we used so far, the ray originates at $l - \epsilon$ and ends after $u + \epsilon$. Thus, the origin of the ray is offset from zero. In **Parallel from zero** (Figure 5b), the ray always originates from 0 and ends after $u + \epsilon$. To avoid false positives, t_{\min} is set to $l - \epsilon$. For point queries, we have a third option available: Using **Perpendicular** (Figure 1), the ray always targets only one specific triangle and is fired from a perpendicular angle to it. Table 2 summarizes the three options we have with their respective ray parameters.

Method	o	d	t_{\min}	t_{\max}
Para. offset (Fig. 5a)	$(l - \epsilon, 0, 0)$	$(1, 0, 0)$	0	$u - l + 2\epsilon$
Para. zero (Fig. 5b)	$(0, 0, 0)$	$(1, 0, 0)$	$l - \epsilon$	$u + \epsilon$
Perpend. (Q3 in Fig. 1)	$(l, 0, -\epsilon)$	$(0, 0, 1)$	0	2ϵ

Table 2: Ray configuration parameters.

In Figure 6, we first evaluate whether point queries should be expressed as a parallel rays or as perpendicular rays. We start the parallel rays from zero, as in Extended Mode, offsetting the origin yields incorrect results due to `float32` precision issues. We can clearly see that perpendicular rays consistently yield better lookup times than parallel rays, as for the former, an intersection test is sufficient to identify a hit, while for the latter, additional comparisons are carried out to ensure $t_{min} < t < t_{max}$.

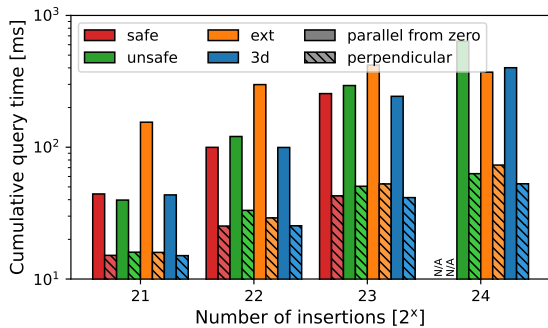


Figure 6: Lookup time for parallel and perpendicular rays.

To identify which choice works better for range queries, in Table 3, we compare the query answering time for offset rays, and rays starting at zero. Note that we evaluate only 3D Mode here, since Extended Mode does not support rays with offset, while Safe/Unsafe Mode does not permit the tested key range of 2^{25} . We can see that offsetting the origin pays off in all cases over keeping the origin at zero.

Number of hits	1	4	16	64	256
Parallel from offset [ms]	61	197	580	2086	8025
Parallel from zero [ms]	61	1209	1652	3382	10196

Table 3: Lookup time for two choices of ray origin for range queries in 3D Mode.

Selected Configuration. RX uses perpendicular rays for point queries and rays with an offset origin for range queries.

3.4 Which Primitive Type Is Ideal?

So far, we have discussed how to express our keys using triangles. However, apart from triangles, OptiX supports other primitive types, namely *spheres* and *axis-aligned bounding boxes (AABBs)*.

Spheres. In contrast to triangles, which are planar, spheres are curved surfaces defined by their center point and their radius. A ray-sphere intersection can only occur when the ray enters or exits the volume of the sphere at some point. To ensure that a ray can always start outside of a sphere, we must avoid packing the spheres too densely. Therefore, we choose $r = \epsilon/2 = 0.25$ as the radius for each sphere. Since the radius is uniform for all spheres, OptiX allows us to specify the radius for all spheres at once. Consequently, each sphere only requires three `float32` to store the center, making this representation comparatively space-efficient.

AABBs. Like spheres, AABBs delimit a volume, and only register an intersection when a ray strikes one of the six faces. AABBs are intended to enclose user-defined primitives, e.g. implicitly defined

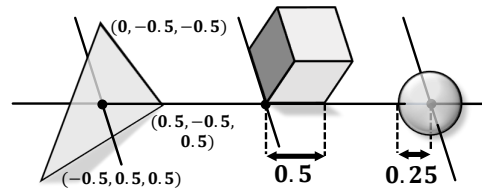


Figure 7: Triangle, AABB, and sphere primitives.

surfaces, allowing them to be part of a larger 3D scene without requiring them to be supported by OptiX natively. Consequently, the user is expected to provide their own *intersection program* to figure out if a ray actually hits the object enclosed by the bounding box. In our case, it is sufficient to move the contents of the any-hit program into the intersection program, and not report a hit in the end. Internally, each AABB is represented by two corner points on opposite sides, making AABBs more space-efficient than triangles.

Let us now compare the accumulated lookup time, the build time, and the memory footprint for all three primitive types in Figure 8. Regarding lookup performance, triangles clearly perform best with a significant margin. We attribute this to the fact that the ray-triangle intersection test is implemented in hardware [13], utilizing the raytracing cores, whereas spheres and AABBs both call a software-based intersection program³. In terms of BVH build time, triangles also perform best, along with AABBs, while sphere BVHs take longer to create. Unfortunately, the memory footprint of (uncompacted) triangles is the highest in comparison.

Selected Configuration. When optimizing for lookup performance, triangles should be preferred in order to fully utilize hardware acceleration. When optimizing for memory footprint, AABBs should also be considered. As we prioritize lookup performance, RX uses triangles in the following.

3.5 To Compact or Not to Compact?

Any BVH created by OptiX can optionally be compacted (via `optixAccelCompact()`) to save space. The compaction process requires a target buffer to write the compacted BVH to. Unfortunately, the OptiX manual does not explain how compaction is actually implemented. However, as the memory region that holds the initial BVH needs to be over-allocated (since the actual size is unknown before the build), we assume that the compaction is simply a copy of the BVH into the target buffer of fitting size.

First, in Figure 8a, we experimentally verify that compaction does not negatively affect lookup performance. In Figure 8b, we can see that compacting the structure after building it is cheap for all three methods. Especially for triangles, the time overhead is negligible. At the same time, in Figure 8c, we can see that the memory footprint decreases by up to 50% under compaction. AABBs take comparatively little space even when not compacted, and thus the impact of compaction is not as significant. Surprisingly, a sphere BVH takes the most time to compact, and the final memory footprint is the largest of the three primitives.

Selected Configuration. Overall, a triangle BVH has the smallest memory footprint (when compacted) and yields the best lookup

³The sphere intersection program is part of a pre-defined OptiX software module, and not user-programmable.

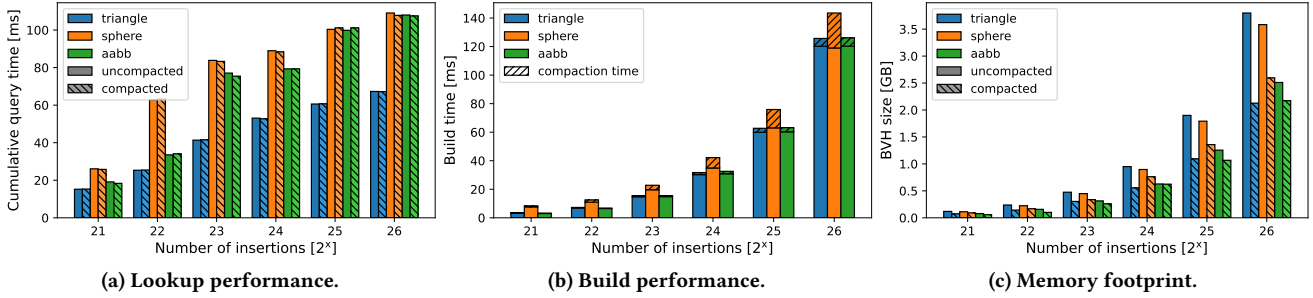


Figure 8: Comparison of primitive types.

performance. Consequently, **RX** always compacts the triangle BVH after construction.

3.6 How Do We Perform Updates?

Next, let us discuss how we can perform updates on an already existing index. Ideally, our index should provide a method of selectively updating entries, or in our case, moving triangles around, which takes less time than a full rebuild.

OptiX natively supports in-place updates to bounding volume hierarchies via `optixAccelBuild()`, albeit with a few restrictions [14]: (1) A special flag has to be set during construction. Setting this flag disables the effects of compaction, i.e. the BVH will always keep its initial size. (2) Updates still require additional temporary memory. (3) Updates cannot add new primitives or remove existing primitives. In the presence of these limitation, it might be a viable option to simply rebuild the index.

To evaluate OptiX’ update behavior, we build the BVH as described earlier and set the aforementioned update flag. We then randomly select a subset of m rows and apply a fixed-point-free permutation to this subset. This effectively simulates m updates, but retains the invariants that (1) all keys are unique, (2) there are no gaps in the key set, and (3) the key order is random. As such, we would expect the lookup time to remain identical after the updates have been performed. Finally, we construct a new triangle buffer from the updated column, and update the BVH via `optixAccelBuild()`. This is followed by the usual lookup phase.

Number of updates	0	64	256	1024	4096	rebuild
Update time [ms]	39.61	39.60	39.55	39.49	39.58	129.05
Query time [ms]	67	67	127	576	4720	196

Table 4: Update time and query time for 2²⁶ keys.

Table 4 shows that for a fixed build size, updates take a constant amount of time, even if the number of updates is zero. Simultaneously, updating is more than three times faster than rebuilding the BVH from scratch. However, the subsequent querying slows down significantly as the number of updates increases: For update sizes above 256, a full rebuild followed by a lookup would still be faster than performing the lookup in the updated BVH. The OptiX documentation confirms this behavior [14], claiming that the quality of the BVH will degrade substantially when too many triangles are relocated.

Selected Configuration. We conclude that updates in **RX** should always be realized via a full rebuild.

4 EXPERIMENTAL EVALUATION

After identifying a reasonable and well-performing configuration, we will now vary the experimental setup along eight dimensions and compare **RX** against three traditional GPU-resident index structures as baselines.

The experimental setup in this section is the same as in Section 3.1, however, instead of restricting the indexed column I to consecutive integers, we now permit the full integer range as keys. Any exceptions to this setup will be stated explicitly. Also note that in all following plots, bars reaching to the top of the plot are not cut off, but actually end there.

4.1 Traditional GPU Indexes as Baselines

We compare against the following GPU-resident index structures:

HT. Our first baseline is WarpCore, a state-of-the-art GPU hashtable by Jünger et al. [26, 27]. WarpCore implements *cooperative probing*, where each key is assigned to a group of threads during inserts or lookups, and each group accesses neighboring slots in the hashtable. This accelerates the task of identifying an empty slot for insertion, or discovering the key to be looked up, while still using the GPU’s cache and load-store units to the maximum extent possible. The authors show that WarpCore outperforms other recent GPU hashtables, such as SlabHash [4] and cuDPP [2, 3], especially when the majority of slots is occupied. The authors then choose a target load factor of 0.8 for all subsequent experiments, therefore, we also use 0.8 as the target load factor in this section. In addition, we fix the group size for cooperative probing to 8, which is the default. Since there is no bulk-loading for hashtables, we insert each key separately during the build phase.

B+. Our second baseline is the state-of-the-art GPU B+-Tree by Awad et al. [6] in its recently updated version [7, 23]. This baseline traverses the tree in groups of 16 threads, so that lookups within a node can be done synchronously using warp intrinsics. The build phase sorts the keys using CUB’s key-value `DeviceRadixSort` [15], an out-of-place GPU radix sort that is considered the fastest way to sort integers using a CUDA-enabled GPU, then bulk-loads the tree with the sorted key-value pairs. Just like **HT**, the B+-Tree also supports regular insertions, but the performance greatly depends on the distribution of the inserted keys, which is not the case when bulk-loading. However, unlike **HT** and **RX**, the B+-Tree only supports 32-bit keys. In comparison to a GPU LSM tree [5], the B+-Tree yields better query performance, making it an ideal baseline for the query-heavy benchmarks in this section. Note that we had to

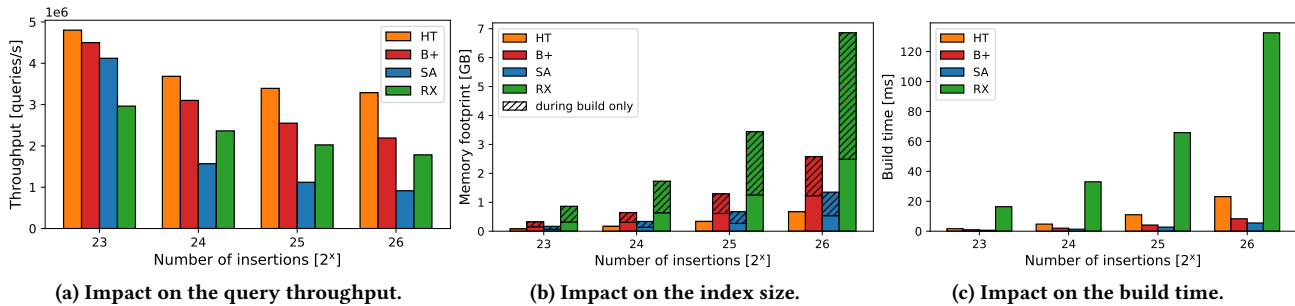


Figure 9: Varying the build size.

slightly modify the range query code for the B+-Tree in order to support efficient aggregation.

SA. Our third baseline is a sorted array, which we combine with a naive binary search for lookups. This mimics the access patterns that would occur during lookups in a balanced binary tree, while requiring less overall memory. Insertions and deletions cannot take place after the index has been constructed. Still, this index is trivial to implement, and serves as a great baseline for more sophisticated approaches. Again, we utilize CUB’s radix sort to sort the array.

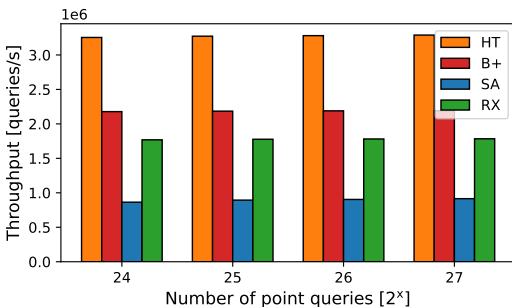


Figure 10: Throughput for a varying number of point queries.

4.2 Varying the Number of Point Queries and the Number of Inserts

We start by analyzing the scaling behavior of the methods. In Figure 10, we first vary the number of point queries on the x -axis from 2²⁴ to 2²⁷ while keeping the number of inserted keys constant at 2²⁶. On the y -axis, we report the throughput in number of answered queries per second. First of all, we observe that all four variants scale linearly with the number of queries, which matches our expectation. We therefore fix the number of queries to 2²⁷ for the remainder of the evaluation. Unsurprisingly, we can also see that **HT** clearly outperforms the remaining indexes under point queries, while **SA** shows by far the worst performance. This discrepancy can be explained by the fact that **HT** and **B+** maximize the number of coalesced memory accesses during lookups, which happen when two neighboring threads access neighboring memory addresses. In contrast, when two neighboring threads simultaneously perform binary searches for distinct keys, they are very likely to access entirely different regions of the sorted array. Overall, this shows that in terms of point query performance, **RX** is indeed competitive in comparison to the other range-query supporting index structures

B+ and **SA**. **HT**, which is specialized for point queries, seems to be unreachable though.

In Figure 9, we reverse this setup, varying the number of inserts from 2²³ to 2²⁶ while keeping the number of point queries constant. In Figure 9a, we can see that for all tested indexes, the throughput only marginally decreases with an increase in the number of inserts, indicating that even for 2²³ keys, caching effects play no role anymore. The relative performance between the indexes does not change significantly when varying the number of inserts. Next, in Figure 9b, we look at the size of the generated index. Here, we differentiate between the required space during construction and the space required afterwards. We can see that **RX** consumes considerably more space during construction than the traditional methods. After construction, the space overhead is noticeably smaller, but still around twice as high as for **B+**. This is likely a consequence of the space-inefficient key representation as nine float32, where other indexes can store each key as-is. **SA** consumes more space than **HT** during construction (caused by the out-of-place radix sort), but has zero structural overhead afterwards. **HT** consumes slightly more due to the 25% over-allocation to achieve the target load factor. In Figure 9c, we see that **RX** also has the highest build time of all methods, showing the major weakness of the approach. This, in combination with the fact that updates perform poorly (see Section 3.6), indicates that **RX** should be used as a read-only index structure primarily.

We want to mention that during testing, we ran into an issue where the first build of **RX** sometimes ran considerably longer than all remaining runs. The CUDA profiler revealed that the affected runs perform some unknown action on the CPU before starting the actual build. This action is likely a deferred initialization step, but it still interfered with our measurements. Therefore, we eliminated the affected first run before computing the averages reported.

4.3 Ordering Inserts and Point Queries

So far, we assumed that the inserted keys are inherently unsorted. However, in practice, the keys could be present in an ordered fashion in the indexed column already. Also, if sorting is cheap, sorting the batch of point queries by their requested key might be beneficial.

We therefore investigate the impact of sorted inserts and/or sorted point queries over the unsorted alternatives. For sorting our queries, we again use CUB’s DeviceRadixSort. We first analyze the impact on the accumulated point query time for all four combinations in Figure 11. Building an index from a sorted column does not yield any performance improvement. This is not surprising since some index structures perform a sorting step as part of the

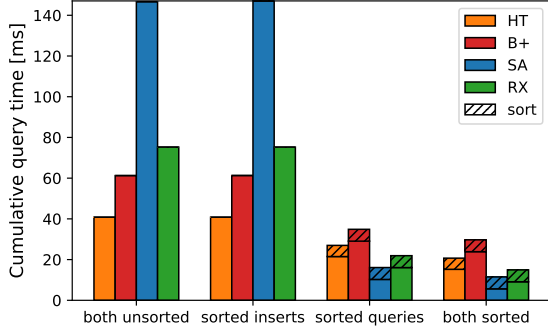


Figure 11: Impact of sorted inserts and point queries on lookup performance.

build process anyway (**B+** and **SA**). However, **HT** and **RX** do not explicitly sort the keys, and still seem unaffected. In contrast, sorting the point queries positively impacts all indexes significantly. This can be attributed to improved locality when traversing the index structure or when loading values from the projected column, since neighboring queries are usually answered simultaneously by neighboring threads. **RX** and **SA** in particular highly benefit from ordered queries, surpassing **B+** and, in the case of **SA**, even **HT**. Also, GPU-resident sorting is surprisingly cheap in comparison to the actual query processing. Note that we also measured the memory footprint as well as the build time under sorted keys. Only **RX** showed a small decrease in build time (8%) when compared to the values in Figure 9c. Also note that sorting in decreasing order instead of increasing order does not have an impact on any method.

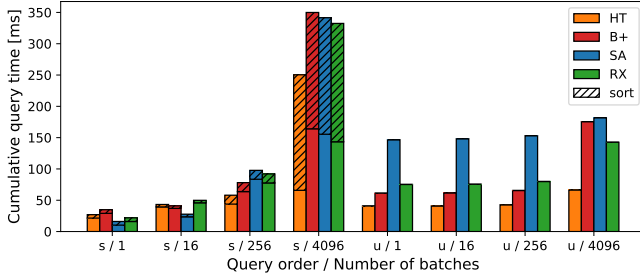


Figure 12: Impact of batching point queries.

4.4 Varying the Batch Size of Point Queries

Until now, we fired a single batch containing all 2^{27} point queries to the index structure in one go. In the following, let us analyze the impact of firing multiple smaller batches, while keeping the total number of queries fixed. A submission pattern of multiple smaller batches occurs in practice if (a) only a limited number of queries are waiting to be answered simultaneously, (b) the query latency is required be small, or (c) we want to sort the queries like in Section 4.2, but there is not enough space available to do it in one go.

Thus, in Figure 12, we vary the number of batches to submit from 1 batch (2^{27} queries per batch) to 4096 batches (2^{15} queries per batch) and report the accumulated point query time on the y -axis. Again, we evaluate both ordered and unordered point queries, as we saw an effect of sorting in Section 4.3. We can see that increasing

the number of batches increases the accumulated query time for all methods. We attribute this effect to the overhead caused by launching more CUDA kernels, since we perform one launch per batch. Interestingly, the performance degrades when sorting the queries, which is especially visible for **RX** and **SA**, where the query time increases by 2x for 4096 queries. In particular, **SA** loses its advantage over **B+** and **RX** under sorted queries for 256 batches. This indicates that in a setting where smaller batches must be handled, **RX** is fully on par with **B+** and **SA**. The sorting overhead also increases considerably, since CUB’s DeviceRadixSort is not designed for sorting small batches.

4.5 Varying the Hit Ratio of Point Queries

Up to this point, we ensured that all queries matched some entry in the table, and therefore, each point query returned a non-empty result. However, depending on the workload, the opposite might be the case: What if the majority of the queried keys did not occur in the table?

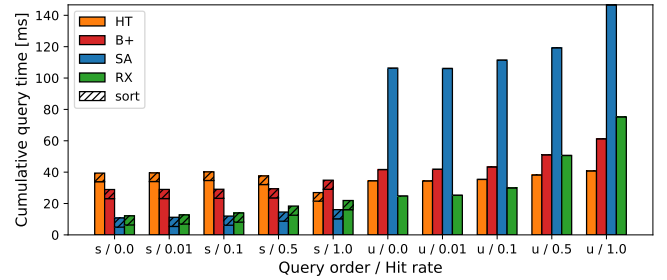


Figure 13: Varying the hit ratio h .

Thus, in Figure 13, we vary the hit ratio h , i.e., the fraction of point queries that return a non-empty result, on the x -axis, and observe the impact on the accumulated point query time on the y -axis. We vary h from only misses ($h = 0$) to few hits ($h = 0.01$, $h = 0.1$) to balanced ($h = 0.5$). For comparison, we include the previously evaluated query sequence consisting of hits only ($h = 1$) as well. Again, we test both unordered and ordered point queries.

With a decrease of h , we observe a notable decrease in query answering time for all indexes except for **HT**. We attribute this to the fact that only hits require us to retrieve a corresponding value from the projected column, whereas each miss can ignore this step. Most notably, **RX** runs disproportionately faster (up to 3x), eventually outperforming its competitors when the hit ratio h drops below 0.1. This is probably caused by an early miss detection when traversing the BVH. Note that this positive effect is even more pronounced when all misses are specifically chosen to lie outside the value range of the key column, i.e. smaller/greater than the smallest/greatest key in the table, which we evaluated additionally: In this case, the BVH can abort traversal at the root node. Interestingly, **HT** does not see an increase in performance with a decrease of the hit ratio, instead, the performance actually decreases. This is likely a consequence of the open addressing scheme built into **HT**, where a miss might result in a lengthy probe sequence in order to detect that the key is not part of the index.

4.6 Range Queries

So far, we solely evaluated point queries, where each query returned at most one result. Here, **HT** unsurprisingly dominated all other

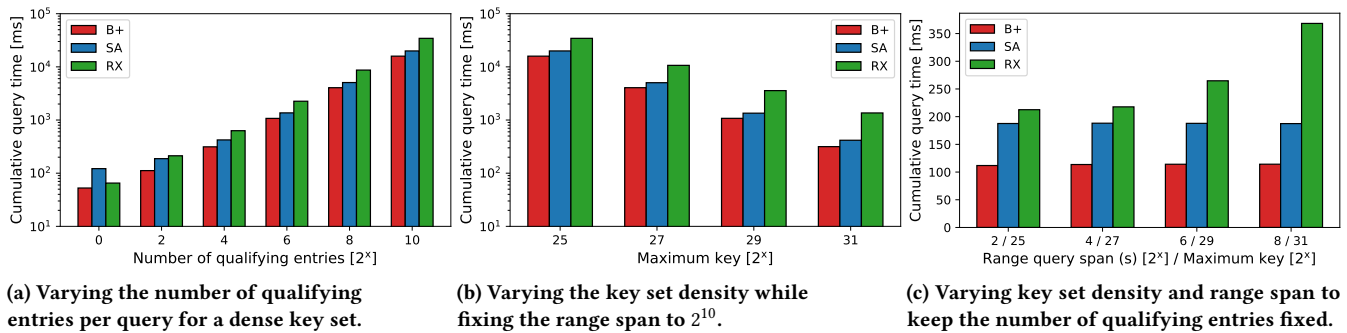


Figure 14: Evaluating the accumulated range query time.

methods. However, as soon as we want to answer range queries, which are not supported by **HT**, the order-based indexes **RX**, **B+**, and **SA** can show their strengths. Thus, in Figure 14, we compare these indexes in terms of accumulated range query performance while varying three different parameters.

In Figure 14a, we vary the number of qualifying entries per query from 2^0 (point queries) to 2^{10} on the x -axis while showing the accumulated range query time for a total of 2^{27} queries on a logarithmic y -axis. To easily generate range queries that return a specific number of qualifying entries, we build each index from a column filled with a dense shuffled key set containing *all* integers in $[0, 2^{25})$. On such a dense key set, a querying the range $[l^{(i)}, u^{(i)}]$ with a span of $s = u^{(i)} - l^{(i)} + 1$ will return exactly s qualifying entries. Note that this setup represents the worst-case scenario for range queries, as all keys within each range actually exist and therefore qualify. Thus, it yields an upper bound for the execution time. From the result, we see that **B+** yields the best performance across all choices of s . **RX** initially outperforms **SA** for small range queries, but then quickly loses its advantage. This can be explained by the fact that both **B+** and **SA** store the keys in an ordered fashion, and therefore, only have to locate the smallest qualifying key in the index. All other qualifying keys can be found by traversing the index structure sideways, until the first non-qualifying key is found. **B+** implements sideways traversal through a linked list of leaf nodes. In addition, **B+** utilizes warp-level aggregation to accelerate the sum, giving it an additional advantage over its competitors. On the other hand, **RX** has to identify each qualifying entry individually. The relative performance between the indexes stabilizes once s exceeds 2^6 , after which the query time truly scales linearly with s .

In Figure 14b, we vary the density of our indexed key set by generating keys within $[0, 2^{25})$ (as in Figure 14a), up to $[0, 2^{31})$, while keeping the total number of indexed keys constant at 2^{25} . We now generate range queries $[l^{(i)}, u^{(i)}]$ such that the range span is fixed to $s = u^{(i)} - l^{(i)} + 1 = 2^{10}$. With a decrease in key set density, this results in a decreasing number of qualifying entries per range query, and consequently, in less work per query. The results confirm that this reduction of work indeed improves the lookup time of each method, but **SA** and **B+** seem to benefit more than **RX**.

The same effect can be seen in Figure 14c, in which we vary the key set density while keeping the number of qualifying entries (i.e. the selectivity) constant. To do so, we test the same key set densities as in Figure 14b, but as the density decreases, we simultaneously increase the range span s such that each query always results in

four qualifying entries on average. Under the assumption that projection and aggregation dominate the execution time, we expect the cumulative time to remain constant, which holds true for **SA** and **B+**, but not for **RX**. This observation is highly unintuitive: For **RX**, a decrease in key density also results in a decrease in triangle density along the x -axis. Consequently, if **RX** fires a ray in parallel to the x -axis, more triangles could be excluded early on, and we would therefore expect the performance to improve. Instead, the drop in performance likely boils down to implementation details in the BVH generation, which we have no control over. As a final note, remember that **RX** starts casting more than two rays per query only when $s > 2^{22}$. Therefore, the poor range query performance of **RX** is certainly not caused by casting unnecessarily large amounts of rays. In fact, if $s > 2^{22}$, a full scan of the table might be faster than using any index at all.

4.7 Impact of the Size of Keys

So far, we focused on 32-bit keys, as **B+** does not support larger keys. However, let us now extend the key size to 64 bits to see how the remaining indexes react.

In Figure 15, we compare the query answering time, index size, and build time for 32-bit and 64-bit keys. We also show the 32-bit results for **B+** as a point of reference. Regarding query performance, Figure 15a shows **SA** and **HT** slowing down under 64-bit keys, which is likely a consequence of the increased cost of 64-bit integer comparisons on GPUs, possibly in combination with the increased memory footprint of the underlying data structure. On the other hand, **RX** is unaffected by the increase in key size, since **RX** does not differentiate between 32-bit keys and 64-bit keys internally.

Figure 15b shows the memory footprint of all indexes. Since **RX** treats 32-bit keys like 64-bit keys during construction, the size of the BVH is mostly the same, apart from small random variations pertaining to the choice of inserted keys. In contrast, both **SA** and **HT** store each key in its original representation, and therefore, 64-bit keys lead to a noticeable increase in memory consumption. The changes in build time (Figure 15c) for **SA** and **HT** can be explained similarly. In addition, **SA** invokes a radix sort during construction, whose execution time depends directly on the number of key bits. Meanwhile, the build times for **RX** are within margin of error.

4.8 Varying the Skew in the Key Distribution

We have seen how the indexes perform on a column of uniformly distributed keys, answering uniformly distributed queries. In the

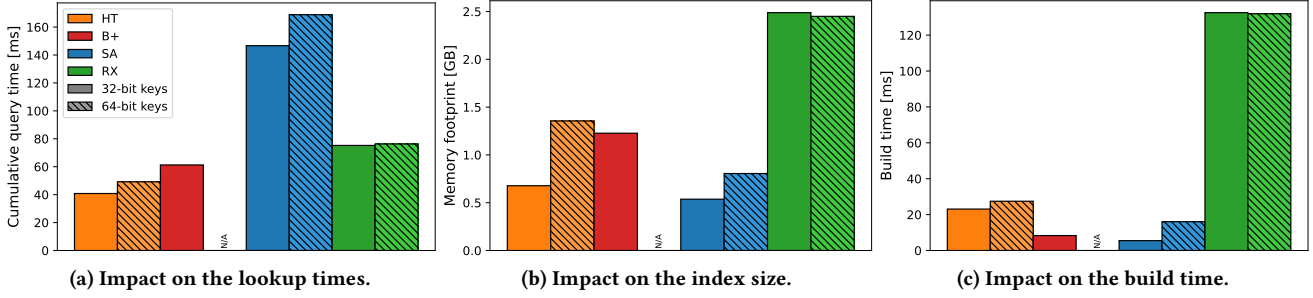


Figure 15: Impact of the key size (32-bit vs 64-bit).

following, we will introduce skew to both the key distribution as well as the query distribution and observe the effects on the indexes.

First, in Figure 16, we introduce skew to the key distribution while retaining a uniform point query distribution (without misses). Again, we evaluate both sorted and unsorted point queries. To introduce skew, we generate a certain portion of the key set densely around the center of the 32-bit key range. The remaining keys are drawn uniformly, but without generating duplicate keys. We vary the portion of densely generated keys from 0.0 (resembling a uniform distribution just like before) up to 1.0 (only dense keys) on the x -axis and report the accumulated query time on the y -axis. From the results we can see that all indexes are almost unaffected by a skewed key set. **RX** shows marginal performance improvements when the keys are densely packed, which is similar to the effect we observed in Section 4.6.

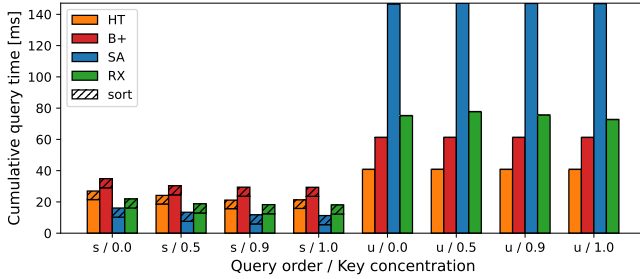


Figure 16: Varying the skew of inserted keys under uniformly distributed point queries.

In Figure 17, we instead introduce skew to the point query distribution, but keep the inserted keys uniform. Here, our point queries follow a Zipf distribution. On the x -axis, we vary the Zipf coefficient from 0.0 (resembling a uniform distribution) up to a very high skew of 2.0 and observe the accumulated query time on the y -axis.

In contrast to the skewed inserts, skewed point queries have a positive effect on the performance. This holds especially for unsorted point queries. We attribute this to an improved access locality under skew, as the queries now focus on a smaller key range. Under sorted queries, the performance improvement is less noticeable, as firing ordered point queries already ensures good access locality (see Section 4.3). We can also see that with sufficient skew, **RX** performs second-best after **SA**. Overall, under unsorted queries, **RX** experiences a speedup of around 15x with skewed queries, while **SA** runs 63x faster. Meanwhile, **B+** only speeds up by 2.5x.

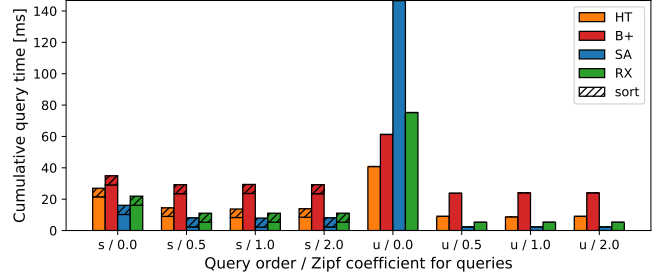


Figure 17: Varying the skew of point queries on uniformly distributed keys.

4.9 Varying the Hardware Architecture

Until now, we evaluated all methods on the most recent Ada Lovelace GPU architecture. By testing the two previous architectures Ampere and Turing, we can find out how much has changed over the generations, in particular regarding the performance delivered by the varying number of available raytracing cores. Table 5 provides an overview of the four test systems spanning three generations of RTX GPUs. While each system features a different CPU model, remember that all measurements are fully GPU-resident, and therefore, CPU performance can barely influence any result.

Sys.	RTX GPU	Architecture	VRAM	RTX cores	CPU
S1	4090	<i>Ada Lovelace</i>	24GB	128	TR 3990X
S2a	A6000	<i>Ampere</i>	48GB	84	i9 12900K
S2b	3090	<i>Ampere</i>	24GB	82	i7 11700K
S3	2080Ti	<i>Turing</i>	11GB	68	i9 9900K

Table 5: Evaluated GPUs and hardware architectures.

In Figure 18, we show the accumulated point query performance for both sorted and unsorted point queries on all four test systems. For all tested index structures, we observe a significant performance improvement over the three hardware generations. However, we can also see that while **RX** was not yet competitive on system **S3**, it is competitive on system **S1**. This clearly shows that **RX** improved the most among all reasonably-performing methods. Precisely, from **S3** to **S1**, **RX** improved by a factor of 3.3, while **HT** improved only by 2.4, and **B+** only by 3.2. **SA** improved by a factor of 4.0, but still performs noticeably worse than all other baselines. We attribute the faster improvement of **RX** to a significant increase in the number and performance of the available raytracing cores. Since this trend

of increasing the number of raytracing cores will likely continue in future generations (such as the upcoming *Grace Hopper* generation), **RX** might be able to outperform the traditional variants eventually.

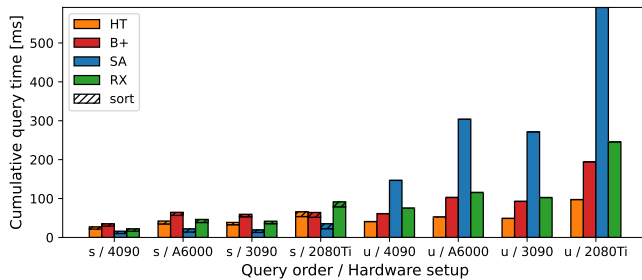


Figure 18: Impact of hardware architecture on lookup times.

5 RELATED WORK

Obviously, NVIDIA RTX was originally designed to accelerate the rendering of complex lighting effects, e.g. transparency, reflection, refraction, and drop shadows, in real-time. However, apart from this paper, there exist other works outside of rendering that utilized hardware acceleration on RTX-enabled GPUs in creative ways.

For example, a line of work uses raytracing to perform *point containment tests* [30, 36, 45, 50]. A point containment test determines whether a point lies inside the boundary of a polygon (in 2D) or a polyhedron (in 3D). One way to implement such a test is by casting a ray in any direction and counting the number of intersections with the boundary, which can be solved efficiently on RTX-enabled GPUs. Another area of application is *time-of-flight imaging* [35, 42, 48]. Time-of-flight sensors compute distances to surrounding objects by measuring the difference between transmission and reception of electromagnetic or acoustic pulses. Specialized software can then recreate a three-dimensional scene from a sufficient number of measurements. To test these systems, researchers can simulate the propagation of pulses produced by such a sensor with hardware-accelerated raytracing in a virtual environment. Also, the problem of performing an efficient *radius search* [19, 54] has been accelerated using RTX. A radius search locates all points within a fixed radius from a specified point. One can improve this search with a bounding volume hierarchy to quickly exclude far-away points, which can be delegated to the RTX cores. Further areas of application include physical simulations for *graph rendering* [51] and *particle movement* [8, 9, 46].

Independent from NVIDIA RTX, in recent years, there is a trend of turning traditional index structures to *GPU-resident index structures*. Typically, this implies optimizations to the memory layout and access patterns, and changes to the memory allocation strategy. Occasionally, a GPU index requires profound algorithmic changes to alleviate contention issues caused by the enormous number of active threads. Note that some existing GPU indexes only allow queries on the GPU, while construction and updates can only run on the host. GPU hashtables [2–4, 25, 26, 32, 52] provide key-value mappings which yield top-of-the-line performance for point queries, but require various degrees of over-allocation to perform efficiently, and cannot answer range queries. If one only needs to test membership, Bloom filters [17, 24, 26] and quotient filters [21] require less

space than hashtables, but membership queries can produce false positives. Radix trees [1] and comparison-based trees [5–7, 29] also manage key-value mappings, but support range queries in addition. Trees generally perform worse than hashtables since tree traversal entails multiple cache misses, and some trees demand sophisticated in-GPU memory managers to dynamically allocate new nodes. While our comparison includes a state-of-the-art comparison-based tree, no code for the radix tree was freely available at the time of writing. If a column is limited to a small amount of discrete values, a GPU bitmap index [44] can also offer fast point and range queries, while keeping a minimal memory footprint. Since we specifically devised **RX** to support all possible 64-bit values in Section 3, a fair comparison with bitmap indexes is not possible. Spatial queries require more specialized solutions, such as GPU R-Trees [39, 49] or GPU permutation indexes [33]. Since R-Trees also employ bounding volumes, it would have been compelling to compare a software R-Tree to our hardware-accelerated BVH approach. Unfortunately, both R-Tree implementations do not disclose their source code. Finally, learned indexes [53] achieve high performance on GPUs, since they heavily depend on linear algebra operations, which have been extensively optimized on GPUs, and some GPUs even offer specialized accelerators for these operations. Regrettably, we were unable to check whether the existing learned index takes advantage of hardware acceleration, as there is no accompanying implementation available.

Apart from indexing on GPUs, there is has been interesting work proposing entirely or partially GPU-resident DBMS architectures [10, 11, 18]. Also, other DBMS operations like joins [20, 31, 34, 38, 40] or grouping and aggregation [28, 43, 47] have been migrated successfully to GPUs.

Finally, we want to mention that apart from OptiX, DirectX [41] and Vulkan [22] also provide APIs targeting hardware-accelerated raytracing. Therefore, our proposed indexing scheme could be implemented in either of these.

6 LESSONS LEARNED & CONCLUSION

We presented **RX** and showed that database indexing can indeed be expressed in a raytracing pipeline to utilize the built-in hardware acceleration of RTX cards. We analyzed four design dimensions and empirically evaluated that by splitting 64-bit keys into three parts (3D Mode) and by using these parts as vertex coordinates for a compacted triangle BVH, we achieve a good tradeoff between space utilization and lookup performance. Also, we identified that point queries should be expressed by perpendicular rays while range queries should be fired with an offset origin for best performance. Further, we discovered that under point queries, **RX** can compete with traditional comparison-based indexes. In high-miss scenarios, **RX** even outperforms all traditional methods, including the hashtable. A higher number of batches, as well as sorting query predicates, is also beneficial for **RX**. However, we also identified that **RX** is currently not competitive with traditional indexes in terms of build time, memory footprint, and support for updates. Thus, **RX** should be used in a read-only fashion. Finally, we have seen that **RX** improves faster than the baselines over the generations, starting from not being competitive to being on par with the baselines on current-gen hardware. If this trend continues (as more

and more raytracing cores will be implemented), **RX** might be able to outperform the baselines on future RTX generations.

Acknowledgement: This work is supported by NVIDIA's Academic Hardware Grant, which provided us with the A6000 GPU.

REFERENCES

- [1] Md. Maksudul Alam, Srikanth B. Yognath, and Kalyan S. Perumalla. 2016. Performance of Point and Range Queries for In-memory Databases Using Radix Trees on GPUs. In *18th IEEE International Conference on High Performance Computing and Communications; 14th IEEE International Conference on Smart City; 2nd IEEE International Conference on Data Science and Systems, HPCC/SmartCity/DSS 2016, Sydney, Australia, December 12-14, 2016*, Jinjun Chen and Laurence T. Yang (Eds.). IEEE Computer Society, 1493–1500. <https://doi.org/10.1109/HPCC-SmartCity-DSS.2016.0212>
- [2] Dan A. Alcantara, Andrei Sharf, Fatemeh Abbasinejad, Shubhabrata Sengupta, Michael Mitzenmacher, John D. Owens, and Nina Amenta. 2009. Real-time parallel hashing on the GPU. *ACM Trans. Graph.* 28, 5 (2009), 154. <https://doi.org/10.1145/1618452.1618500>
- [3] Dan A. Alcantara, Vasily Volkov, Shubhabrata Sengupta, Michael Mitzenmacher, John D. Owens, and Nina Amenta. 2012. Chapter 4 - Building an Efficient Hash Table on the GPU. In *GPU Computing Gems Jade Edition*, Wen mei W. Hwu (Ed.). Morgan Kaufmann, Boston, 39–53. <https://doi.org/10.1016/B978-0-12-385963-1.00004-6>
- [4] Saman Ashkiani, Martin Farach-Colton, and John D. Owens. 2018. A Dynamic Hash Table for the GPU. In *2018 IEEE International Parallel and Distributed Processing Symposium, IPDPS 2018, Vancouver, BC, Canada, May 21-25, 2018*. IEEE Computer Society, 419–429. <https://doi.org/10.1109/IPDPS.2018.00052>
- [5] Saman Ashkiani, Shengren Li, Martin Farach-Colton, Nina Amenta, and John D. Owens. 2018. GPU LSM: A Dynamic Dictionary Data Structure for the GPU. In *2018 IEEE International Parallel and Distributed Processing Symposium, IPDPS 2018, Vancouver, BC, Canada, May 21-25, 2018*. IEEE Computer Society, 430–440. <https://doi.org/10.1109/IPDPS.2018.00053>
- [6] Muhammad A. Awad, Saman Ashkiani, Rob Johnson, Martin Farach-Colton, and John D. Owens. 2019. Engineering a high-performance GPU B-Tree. In *Proceedings of the 24th ACM SIGPLAN Symposium on Principles and Practice of Parallel Programming, PPoPP 2019, Washington, DC, USA, February 16-20, 2019*, Jeffrey K. Hollingsworth and Idit Keidar (Eds.). ACM, 145–157. <https://doi.org/10.1145/3293883.3295706>
- [7] Muhammad A. Awad, Serban D. Porumbescu, and John D. Owens. 2022. A GPU Multiversion B-Tree. In *Proceedings of the International Conference on Parallel Architectures and Compilation Techniques, PACT 2022, Chicago, Illinois, October 8-12, 2022*, Andreas Klöckner and José Moreira (Eds.). ACM, 481–493. <https://doi.org/10.1145/3559009.3569681>
- [8] Pascal R. Bähr, Bruno Lang, Peer Ueberholz, Marton Ady, and Roberto Kersevan. 2022. Development of a hardware-accelerated simulation kernel for ultra-high vacuum with Nvidia RTX GPUs. *Int. J. High Perform. Comput. Appl.* 36, 2 (2022), 141–152. <https://doi.org/10.1177/10943420211056654>
- [9] Blyth, Simon. 2020. Meeting the challenge of JUNO simulation with Opticks: GPU optical photon acceleration via NVIDIA OptiX™. *EPJ Web Conf.* 245 (2020), 11003. <https://doi.org/10.1051/epjconf/202024511003>
- [10] Nils Boesch and Carsten Binnig. 2022. GaccO - A GPU-accelerated OLTP DBMS. In *SIGMOD '22: International Conference on Management of Data, Philadelphia, PA, USA, June 12 - 17, 2022*, Zachary Ives, Angela Bonifati, and Amr El Abbadi (Eds.). ACM, 1003–1016. <https://doi.org/10.1145/3514221.3517876>
- [11] Periklis Chrysogelos, Manos Karpotiaktakis, Raja Appuswamy, and Anastasia Ailamaki. 2019. HetExchange: Encapsulating heterogeneous CPU-GPU parallelism in JIT compiled engines. *Proc. VLDB Endow.* 12, 5 (2019), 544–556. <https://doi.org/10.14778/3303753.3303760>
- [12] Microsoft Corporation. 2022. DirectX Raytracing. <https://microsoft.github.io/DirectX-Specs/d3d/Raytracing.html#ray-extents> Accessed: February 27, 2023.
- [13] NVIDIA Corporation. 2018. NVIDIA Turing Architecture In-Depth. <https://developer.nvidia.com/blog/nvidia-turing-architecture-in-depth/> Accessed: February 27, 2023.
- [14] NVIDIA Corporation. 2019. Dynamic Updates. https://raytracing-docs.nvidia.com/optix7/guide/index.html#acceleration_structures#dynamic-updates Accessed: February 27, 2023.
- [15] NVIDIA Corporation. 2022. CUB. <https://nvlabs.github.io/cub/> Accessed on February 27th, 2023.
- [16] NVIDIA Corporation. 2023. NVIDIA OptiX. <https://developer.nvidia.com/rtx/raytracing/optix> Accessed: February 27, 2023.
- [17] Lauro B. Costa, Samer Al-Kiswany, and Matei Ripeanu. 2009. GPU support for batch oriented workloads. In *28th International Performance Computing and Communications Conference, IPCCC 2009, 14-16 December 2009, Phoenix, Arizona, USA*. IEEE Computer Society, 231–238. <https://doi.org/10.1109/IPCCC.2009.5403809>
- [18] Harish Doraiswamy and Juliana Freire. 2022. SPADE: GPU-Powered Spatial Database Engine for Commodity Hardware. In *38th IEEE International Conference on Data Engineering, ICDE 2022, Kuala Lumpur, Malaysia, May 9-12, 2022*. IEEE, 2669–2681. <https://doi.org/10.1109/ICDE53745.2022.00245>
- [19] I. Evangelou, G. Papaioannou, K. Vardis, and A. A. Vasilakis. 2021. Fast Radius Search Exploiting Ray Tracing Frameworks. *Journal of Computer Graphics Techniques (JCGT)* 10, 1 (5 February 2021), 25–48. <http://jcgct.org/published/0010/01/02/>
- [20] Hao Gao and Nikolai Sakharnykh. 2021. Scaling Joins to a Thousand GPUs. In *International Workshop on Accelerating Analytics and Data Management Systems Using Modern Processor and Storage Architectures, ADMS@VLDB 2021, Copenhagen, Denmark, August 16, 2021*, Rajesh Bordawekar and Tirthankar Lahiri (Eds.). 55–64. http://www.adms-conf.org/2021-camera-ready/gao_adms21.pdf
- [21] Afton Geil, Martin Farach-Colton, and John D. Owens. 2018. Quotient Filters: Approximate Membership Queries on the GPU. In *2018 IEEE International Parallel and Distributed Processing Symposium, IPDPS 2018, Vancouver, BC, Canada, May 21-25, 2018*. IEEE Computer Society, 451–462. <https://doi.org/10.1109/IPDPS.2018.00055>
- [22] Khronos Group. 2020. Ray Tracing in Vulkan. <https://www.khronos.org/blog/raytracing-in-vulkan> Accessed: February 27, 2023.
- [23] Owens Research Group. 2021. MVGPuBTree: Multi-Value GPU B-Tree. <https://github.com/owensgroup/MVGPuBTree> Accessed: February 27, 2023.
- [24] Masatoshi Hayashikawa, Koji Nakano, Yasuaki Ito, and Ryota Yasudo. 2019. Folded Bloom Filter for High Bandwidth Memory, with GPU Implementations. In *2019 Seventh International Symposium on Computing and Networking, CANDAR 2019, Nagasaki, Japan, November 25-28, 2019*. IEEE, 18–27. <https://doi.org/10.1109/CANDAR.2019.00011>
- [25] Daniel Jünger, Christian Hundt, and Bertil Schmidt. 2018. WarpDrive: Massively Parallel Hashing on Multi-GPU Nodes. In *2018 IEEE International Parallel and Distributed Processing Symposium, IPDPS 2018, Vancouver, BC, Canada, May 21-25, 2018*. IEEE Computer Society, 441–450. <https://doi.org/10.1109/IPDPS.2018.00054>
- [26] Daniel Jünger, Robin Kobus, André Müller, Christian Hundt, Kai Xu, Weiguo Liu, and Bertil Schmidt. 2020. WarpCore: A Library for fast Hash Tables on GPUs. In *27th IEEE International Conference on High Performance Computing, Data, and Analytics, HiPC 2020, Pune, India, December 16-19, 2020*. IEEE, 11–20. <https://doi.org/10.1109/HiPC50609.2020.00015>
- [27] Daniel Jünger. 2022. warpcore. <https://github.com/sleepyjack/warpcore> Accessed: February 27, 2023.
- [28] Tomas Karnagel, René Müller, and Guy M. Lohman. 2015. Optimizing GPU-accelerated Group-By and Aggregation. In *International Workshop on Accelerating Data Management Systems Using Modern Processor and Storage Architectures - ADMS 2015, Kohala Coast, Hawaii, USA, August 31, 2015*, Rajesh Bordawekar, Tirthankar Lahiri, Bugra Gedik, and Christian A. Lang (Eds.). 13–24. <http://www.adms-conf.org/2015/gpu-optimizer-camera-ready.pdf>
- [29] Changkyu Kim, Jatin Chhugani, Nadathur Satish, Eric Sedlar, Anthony D. Nguyen, Tim Kaldewey, Victor W. Lee, Scott A. Brandt, and Pradeep Dubey. 2010. FAST: fast architecture sensitive tree search on modern CPUs and GPUs. In *Proceedings of the ACM SIGMOD International Conference on Management of Data, SIGMOD 2010, Indianapolis, Indiana, USA, June 6-10, 2010*, Ahmed K. Elmagarmid and Divyakant Agrawal (Eds.). ACM, 339–350. <https://doi.org/10.1145/1807167.1807206>
- [30] Moritz Laass. 2021. Point in Polygon Tests Using Hardware Accelerated Ray Tracing. In *SIGSPATIAL '21: 29th International Conference on Advances in Geographic Information Systems, Virtual Event / Beijing, China, November 2-5, 2021*, Xiaofeng Meng, Fusheng Wang, Chang-Tien Lu, Yan Huang, Shashi Shekhar, and Xing Xie (Eds.). ACM, 666–667. <https://doi.org/10.1145/3474717.3486796>
- [31] Zhuohang Lai, Xibo Sun, Qiong Luo, and Xiaolong Xie. 2022. Accelerating multi-way joins on the GPU. *VLDB J.* 31, 3 (2022), 529–553. <https://doi.org/10.1007/s00778-021-00708-y>
- [32] Yuchen Li, Qiwei Zhu, Zheng Lyu, Zhongdong Huang, and Jianling Sun. 2021. DyCuckoo: Dynamic Hash Tables on GPUs. In *37th IEEE International Conference on Data Engineering, ICDE 2021, Chania, Greece, April 19-22, 2021*. IEEE, 744–755. <https://doi.org/10.1109/ICDE51399.2021.00070>
- [33] Mariela Lopresti, Fabiana Piccoli, and Nora Reyes. 2021. GPU Permutation Index: Good Trade-Off Between Efficiency and Results Quality. In *Computer Science - CACIC 2021 - 27th Argentine Congress, CACIC 2021, Salta, Argentina, October 4-8, 2021, Revised Selected Papers (Communications in Computer and Information Science)*, Patricia Pesado and Gustavo Gil (Eds.), Vol. 1584. Springer, 183–200. https://doi.org/10.1007/978-3-031-05903-2_13
- [34] Vasilis Mageirakos, Riccardo Mancini, Srinivas Karthik, Bikash Chandra, and Anastasia Ailamaki. 2022. Efficient GPU-accelerated Join Optimization for Complex Queries. In *38th IEEE International Conference on Data Engineering, ICDE 2022, Kuala Lumpur, Malaysia, May 9-12, 2022*. IEEE, 3190–3193. <https://doi.org/10.1109/ICDE53745.2022.00295>
- [35] Mogamat Yaaseen Martin, Simon Lucas Winberg, Mohammed Yunus Abdul Gaffar, and David MacLeod. 2022. The Design and Implementation of a Raytracing Algorithm for Signal-level Pulsed Radar Simulation Using the NVIDIA® OptiX™ Engine. *J. Commun.* 17, 9 (2022), 761–768. <https://doi.org/10.12720/>

- jcm.17.9.761-768
- [36] Nate Morrical, Ingo Wald, Will Usher, and Valerio Pascucci. 2022. Accelerating Unstructured Mesh Point Location With RT Cores. *IEEE Trans. Vis. Comput. Graph.* 28, 8 (2022), 2852–2866. <https://doi.org/10.1109/TVCG.2020.3042930>
- [37] Steven G. Parker, James Bigler, Andreas Dietrich, Heiko Friedrich, Jared Hoberock, David P. Luebke, David K. McAllister, Morgan McGuire, R. Keith Morley, Austin Robison, and Martin Stich. 2010. OptiX: a general purpose ray tracing engine. *ACM Trans. Graph.* 29, 4 (2010), 66:1–66:13. <https://doi.org/10.1145/1778765.1778803>
- [38] Johns Paul, Shengliang Lu, Bingsheng He, and Chiew Tong Lau. 2021. MG-Join: A Scalable Join for Massively Parallel Multi-GPU Architectures. In *SIGMOD '21: International Conference on Management of Data, Virtual Event, China, June 20-25, 2021*, Guoliang Li, Zhanhuai Li, Stratos Idreos, and Divesh Srivastava (Eds.). ACM, 1413–1425. <https://doi.org/10.1145/3448016.3457254>
- [39] Sushil K. Prasad, Michael McDermott, Xi He, and Satish Puri. 2015. GPU-based Parallel R-tree Construction and Querying. In *2015 IEEE International Parallel and Distributed Processing Symposium Workshop, IPDPS 2015, Hyderabad, India, May 25-29, 2015*. IEEE Computer Society, 618–627. <https://doi.org/10.1109/IPDPSW.2015.127>
- [40] Ran Rui, Hao Li, and Yi-Cheng Tu. 2020. Efficient Join Algorithms For Large Database Tables in a Multi-GPU Environment. *Proc. VLDB Endow.* 14, 4 (2020), 708–720. <https://doi.org/10.14778/3436905.3436927>
- [41] Microsoft DirectX Team. 2018. Announcing Microsoft DirectX Raytracing! <https://devblogs.microsoft.com/directx/announcing-microsoft-directx-raytracing/> Accessed: February 27, 2023.
- [42] Peter Thoman, Markus Wippler, Robert Hranitzky, and Thomas Fahringer. 2020. RTX-RSim: Accelerated Vulkan Room Response Simulation for Time-of-Flight Imaging. In *Proceedings of the International Workshop on OpenCL (Munich, Germany) (IWOCCL '20)*. Association for Computing Machinery, New York, NY, USA, Article 17, 11 pages. <https://doi.org/10.1145/3388333.3388662>
- [43] Diego G. Tomé, Tim Gubner, Mark Raasveldt, Eyal Rozenberg, and Peter A. Boncz. 2018. Optimizing Group-By and Aggregation using GPU-CPU Co-Processing. In *International Workshop on Accelerating Analytics and Data Management Systems Using Modern Processor and Storage Architectures, ADMS@VLDB 2018, Rio de Janeiro, Brazil, August 27, 2018*, Rajesh Bordawekar and Tirthankar Lahiri (Eds.). 1–10. http://www.adms-conf.org/2018-camera-ready/tome_groupby.pdf
- [44] Brandon Tran, Brennan Schaffner, Joseph M. Myre, Jason Sawin, and David Chiu. 2021. Exploring Means to Enhance the Efficiency of GPU Bitmap Index Query Processing. *Data Sci. Eng.* 6, 2 (2021), 209–228. <https://doi.org/10.1007/s41019-020-00148-8>
- [45] Ingo Wald, Will Usher, Nathan Morrical, Laura Lediaev, and Valerio Pascucci. 2019. RTX Beyond Ray Tracing: Exploring the Use of Hardware Ray Tracing Cores for Tet-Mesh Point Location. In *High-Performance Graphics 2019 - Short Papers, Strasbourg, France, July 8-10, 2019*, Markus Steinberger and Theresa Foley (Eds.). Eurographics Association, 7–13. <https://doi.org/10.2312/hpg.20191189>
- [46] Bin Wang, Ingo Wald, Nate Morrical, Will Usher, Lin Mu, Karsten E. Thompson, and Richard Hughes. 2022. An GPU-accelerated particle tracking method for Eulerian-Lagrangian simulations using hardware ray tracing cores. *Comput. Phys. Commun.* 271 (2022), 108221. <https://doi.org/10.1016/j.cpc.2021.108221>
- [47] Kaibo Wang, Kai Zhang, Yuan Yuan, Siyuan Ma, Rubao Lee, Xiaoning Ding, and Xiaodong Zhang. 2014. Concurrent Analytical Query Processing with GPUs. *Proc. VLDB Endow.* 7, 11 (2014), 1011–1022. <https://doi.org/10.14778/2732967.2732976>
- [48] Qiang Wang, Bo Peng, Ziyuan Cao, Xing Huang, and Jingfeng Jiang. 2020. A Real-time Ultrasound Simulator Using Monte-Carlo Path Tracing in Conjunction with Optix Engine. In *2020 IEEE International Conference on Systems, Man, and Cybernetics, SMC 2020, Toronto, ON, Canada, October 11-14, 2020*. IEEE, 3661–3666. <https://doi.org/10.1109/SMC42975.2020.9283057>
- [49] Simin You, Jianting Zhang, and Le Gruenwald. 2013. Parallel spatial query processing on GPUs using R-trees. In *Proceedings of the 2nd ACM SIGSPATIAL International Workshop on Analytics for Big Geospatial Data, BigSpatial@SIGSPATIAL 2013, Nov 4th, 2013, Orlando, FL, USA*, Varun Chandola and Ranga Raju Vatsavai (Eds.). ACM, 23–31. <https://doi.org/10.1145/2534921.2534949>
- [50] Stefan Zellmann, Daniel Seifried, Nate Morrical, Ingo Wald, Will Usher, Jamie A. P. Law-Smith, Stefanie Walch-Gassner, and André Hinkenjann. 2022. Point Containment Queries on Ray-Tracing Cores for AMR Flow Visualization. *Comput. Sci. Eng.* 24, 2 (2022), 40–51. <https://doi.org/10.1109/MCSE.2022.3153677>
- [51] Stefan Zellmann, Martin Weier, and Ingo Wald. 2020. Accelerating Force-Directed Graph Drawing with RT Cores. In *31st IEEE Visualization Conference, IEEE VIS 2020 - Short Papers, Virtual Event, USA, October 25-30, 2020*. IEEE, 96–100. <https://doi.org/10.1109/VIS47514.2020.00026>
- [52] Kai Zhang, Kaibo Wang, Yuan Yuan, Lei Guo, Rubao Lee, and Xiaodong Zhang. 2015. Mega-KV: A Case for GPUs to Maximize the Throughput of In-Memory Key-Value Stores. *Proc. VLDB Endow.* 8, 11 (2015), 1226–1237. <https://doi.org/10.14778/2809974.2809984>
- [53] Xun Zhong, Yong Zhang, Yu Chen, Chao Li, and Chunxiao Xing. 2022. Learned Index on GPU. In *38th IEEE International Conference on Data Engineering Workshops, ICDE Workshops 2022, Kuala Lumpur, Malaysia, May 9, 2022*. IEEE, 117–122. <https://doi.org/10.1109/ICDEW55742.2022.00024>
- [54] Yuhao Zhu. 2022. RTNN: accelerating neighbor search using hardware ray tracing. In *PPoPP '22: 27th ACM SIGPLAN Symposium on Principles and Practice of Parallel Programming, Seoul, Republic of Korea, April 2 - 6, 2022*, Jaejin Lee, Kunal Agrawal, and Michael F. Spear (Eds.). ACM, 76–89. <https://doi.org/10.1145/3503221.3508409>